

PROCEEDINGS OF SPIE

SPIEDigitalLibrary.org/conference-proceedings-of-spie

A comparison of methods for estimating the line spread function of a CT imaging system

Abboud, Samir, Lee, Kristina, Vinehout, Kaleb, Paquerault, Sophie, Kyprianou, Iacovos

Samir Abboud, Kristina Lee, Kaleb Vinehout, Sophie Paquerault, Iacovos S. Kyprianou, "A comparison of methods for estimating the line spread function of a CT imaging system," Proc. SPIE 7961, Medical Imaging 2011: Physics of Medical Imaging, 79615V (16 March 2011); doi: 10.1117/12.877665

SPIE.

Event: SPIE Medical Imaging, 2011, Lake Buena Vista (Orlando), Florida, United States

A comparison of methods for estimating the line spread function of a CT imaging system

Samir Abboud,^{*‡} Kristina Lee,[†] Kaleb Vinehout[†], Sophie Paquerault^{*} and Iakovos S. Kyprianou^{*§}

^{*} Division of Imaging and Applied Mathematics, Center For Devices and Radiological Health, US Food and Drug Administration

[†] Department of Biomedical engineering, Marquette University

[‡] School of Medicine, University of Maryland at Baltimore

[§] Department of Bioengineering, University of Maryland at College Park

ABSTRACT

A quantitative description of the deterministic properties of a CT system is necessary when evaluating image quality. The most common such metric is the modulation transfer function (MTF), usually calculated from a line spread function (LSF) or point spread function (PSF). Currently, there exist many test objects used to measure the LSF or PSF. In this paper we report on a comparison of these measures using; a thin foil slit test object, a teflon cube edge test object and a novel “negative” cube test object. Images were acquired using a custom-built bench-top flat-panel-based cone-beam CT scanner and a cylindrical water-filled PMMA phantom with the test objects embedded in the middle. From the 3-dimensional reconstructed volumes, we estimated the LSF either directly or as estimated from the edge spread function. From these, a modulation transfer function can be estimated, and the frequency dependent image transfer of each object can be reported.

1. INTRODUCTION

There is a wide variety of imaging technologies that can produce images through which a clinician can look into the body to diagnose, monitor or treat diseases or any abnormal health conditions. Unfortunately, there is no imaging technology that can reveal everything on the same image, and different technologies often reveal different characteristics of the patient diseases or conditions. Image quality can considerably differ with the characteristics of the imaging technology and can also be compromised with technique factors such as patient radiation exposure and imaging time. It is therefore important to evaluate and understand image quality and limitations of each technology¹ as well as to develop robust methodologies for measuring image quality.

Since the early 1970s, clinical practice has been revolutionized by the introduction of computed tomography (CT) systems that provide high quality images which reproduce axial cross sections of the body. This led to an improvement in patient care, a better understanding of patient diseases and health conditions, as well as opening new paths in research for disease treatment. CT systems offered without a doubt novel and substantially better imaging of the body (especially for soft tissues), but at the expense of a relatively high radiation exposure compared to other imaging modalities. As rapid technological developments have been realized, there has been a continuing expansion of CT practice. In the last decades, the number of examinations (and thus patient and population exposure from medical x-rays) have substantially increased to the extent that it has recently raised serious concerns. Due to the relative complexity and range of possibilities of CT scanner settings by comparison to conventional radiography, the levels of image quality and patient dose may vary significantly. Thus there is a need to establish guidelines, quality criteria, and standards for CT so that the necessary clinical information

Contact: US Food and Drug Administration. 10903 New Hampshire Ave. W062-3109, Silver Spring, Maryland, 20993-0002, USA. email: samir.abboud@fda.hhs.gov

“The mention of commercial products herein is not to be construed as either an actual or implied endorsement of such products by the Department of Health and Human Services.”

in its optimal form be provided with minimum dose to the patient. Many research groups, such as those from academia, health care providers, device manufacturers, and regulatory entities are engaged in the development of quality criteria for CT, general principles for imaging techniques, quality control of equipment performance as well as methods and materials for measuring the quality of medical images resulting from these imaging systems.

As with many other domains of imaging science, the quality of a medical image is not a single factor but is an ensemble of factors that should be accounted for, including: contrast, sharpness (i.e., blur and visibility of detail), noise, artifacts, and distortion. All of these factors, even though interdependent, are equally important to measure as they allow understanding the full capabilities and limitations of an imaging system. In this paper, we focus on the sharpness factor for a nonlinear system. Sharpness describes the clarity/visibility of detail in an image; both resolution and acutance (or edge contrast) contribute to sharpness. Proper image acquisition settings as well as post-processing image techniques can go a long way towards improving sharpness, even though sharpness is ultimately limited by the imaging system. Image sharpness is usually characterized and reported as a spread function, often with additional calculation of a modulation transfer function (MTF),²⁻⁴ which is defined as the two-dimensional Fourier transform of a point spread function (PSF), the one-dimensional Fourier transform of a line spread function (LSF), or a Fourier transform of the derivative of an edge spread function (ESF).⁵⁻⁷ When comparing sharpness of two imaging systems, and thus their MTFs, it is necessary to calibrate among techniques, i.e., PSF or LSF or ESF, for obtaining the MTF. Previous work exists comparing the different techniques in theory⁸ and in projection imaging.² However, it appeared through a review of the literature that such an intercomparison of these different techniques has not yet been reported for computed tomography (CT) systems. In this paper, we investigate such a comparison of the LSF and ESF techniques of a CT system through preliminary use of specifically designed phantoms (also called test objects in the manuscript).

2. METHODS

2.1 Test objects

Four test objects were used in this study: two thin foil objects for the slit method, and two different cubes for the edge method.* The two foil test devices were constructed of a foil sandwiched between two 2.54 cm thick polymethylmethacrylate (PMMA) plates (Figure 1 illustrates a top and side view of this object). One foil was 0.025 mm thick molybdenum, while the second was 0.1 mm thick aluminum. One cube test object was constructed of a polytetrafluoroethylene (teflon) block with dimensions 2.0 cm × 2.0 cm × 5.0 cm (Figure 2). This will be referred to as the “positive” edge object because it has a higher attenuation than the surrounding material. Teflon was chosen for its radiodensity property in the energy range of interest that was hoped would be suitable for providing a sharp edge while reducing the amount of beam-hardening artifacts. A “negative” cube test object was newly designed and consisted of a cube of air that was bounded on all six sides by polished 2.54 cm thick PMMA blocks, thus creating an edge with lower attenuation than the surrounding material. Four blocks with dimensions 2.54 cm × 2.54 cm × 5.08 cm were assembled as shown in Figure 3. The resulting square was capped on either side by a 7.62 cm × 7.62 cm × 2.54 cm block of PMMA, resulting in a trapped cube of air. This was done to reduce the introduction of beam-hardening artifacts into the CT reconstruction that are frequently seen with materials of high attenuation, while still allowing for an interface with a large difference in attenuation. All of the test objects were placed at the center of a water filled 14 cm PMMA cylinder for imaging, resting on a PMMA stage. The PMMA cylinder had built in tracking beads on the top and bottom parts for geometrical correction of acquired images of the test object. Figure 4 shows the experimental setting of a test object placed in the PMMA cylinder for an imaging acquisition. The two cube test objects were positioned such that the top surface was slightly slanted from the plane normal to the rotation axis, also known as the axial plane. This was done so that the slanted edge method can be used for generating the LSF in the direction parallel to the object rotation axis.

*Here we use the projection radiography terms for slit and edge since the reconstruction of a foil test object results in a line pattern similar to one generated by a slit in projection radiography, while the reconstruction of a cube test object results in a square pattern similar to one generated by an edge in projection radiography.

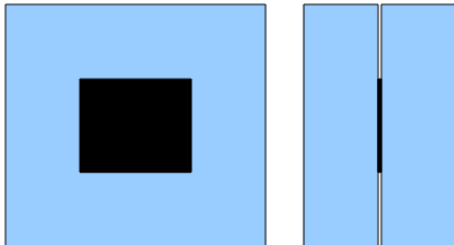


Figure 1: Schematic representation of the foil test object. The PMMA plates are $5.0\text{ cm} \times 5.0\text{ cm} \times 2.54\text{ cm}$.

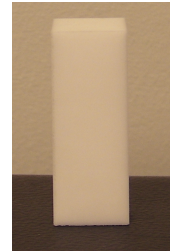


Figure 2: Photograph of the cube test object. This is a polytetrafluoroethylene (Teflon) block with dimensions $2.0\text{ cm} \times 2.0\text{ cm} \times 5.0\text{ cm}$.

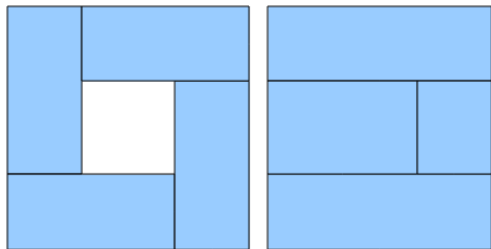


Figure 3: Assembly of the negative cube test object. Four blocks of $2.54\text{ cm} \times 2.54\text{ cm} \times 5.08\text{ cm}$ are assembled as shown on the left to create a square of air, which is then capped on either side by a $7.62\text{ cm} \times 7.62\text{ cm} \times 2.54\text{ cm}$ block to create a trapped cube.



Figure 4: The PMMA cylinder filled with water, shown with the tracking beads for geometrical alignment corrections.

2.2 Image acquisition

All images were acquired using a custom-built bench-top flat-panel-based cone-beam CT scanner.⁹⁻¹¹ The detector used was a Varian 4030CB (Varian Corp., Salt lake City, UT) with 2046×1536 pixels, with 0.195 mm pixel size and a 0.6 mm columnar CsI(Tl) scintillator. The x-ray tube was a Varian B180 with an inherent filtration of 1 mm Al with 0.3 and 0.6 mm nominal focal spots. By using additional filtration of 0.25 mm Ytterbium and a tube voltage of 100 kV, we took advantage of the k-edge emissions of Tungsten (W), which allowed us to generate a quasi monochromatic beam at about 59 keV.¹⁰ For all the data collection we used the 0.6 mm focal spot.

2.3 Data correction and reconstruction

The raw projection images were calibrated to correct for non-uniform gain, non-responsive pixels and the heel effect. Then, the calibrated images were geometrically corrected using a method based on estimating the inclination angles of each detected bead track over the entire CT acquisition.¹² Following all image corrections, 3D volume data were reconstructed with a cubic voxel size of 0.1 mm, using a parallel implementation of the Feldkamp filtered back projection algorithm.

2.4 Line and Edge spread function estimation and comparison

The estimation of the presampled LSF was consistent with previously described computational methods.³ The volumes were reconstructed such that the edges of the object make a small angle with the x and y axes, as shown in figures 5, 10, 13, and 15. It was not necessary to know this angle exactly prior to reconstruction, only that it be between 1 and 3 degrees. At each edge, a region of interest was selected far enough from the corners such that boundary effects could be ignored. One such region from the image of the positive phantom is shown in figure 6. Each row from such an ROI was taken as an estimate of the ESF of this system. However, the resolution of a single row was limited by the voxel size of the image. Because of the tilt of the object, each row was out of phase of the preceding row by a factor defined by the tilt angle. The edge of the cube test object in the region of interest was detected by taking the derivative in the direction normal to the edge, and a line was fit to the resulting maxima of the edge derivative. The slope of this line determines the offset between consecutive rows. ESFs from the out-of-phase rows are shown in figure 7, and the same data is shown in figure 8 after the offset was applied. At this point, our ESF data was no longer limited by the voxel size, but still suffers from noise, especially in the regions away from the edge. Because the angle of the edge was small, the resulting in-phase ESF data was very dense (in this case, roughly 1000 data points per voxel). It was thus reasonable to reduce the noise by averaging neighboring points (here we average every ten neighbors for both location and grayscale value), with the resulting smoothed ESF shown in figure 9. A similar process was used to obtain the voxel-size-independent estimate of the LSF from the foil test object, only in this case the derivative operation was not necessary. These ESFs and LSFs can then be used in estimating the MTF.

For intercomparison among methods the ESF curves were converted to LSF curves. This was done by taking the derivative of the image prior to determining the high resolution spread function. The procedure described above was then used to find the voxel-size-independent estimate of the LSF and reduce noise.

3. RESULTS

Figure 5 shows the average of 100 axial sections of the reconstructed positive test object. Beam-hardening artifacts are present near the edge. Figure 9 shows the average, smoothed ESF from one such ROI; ripples from artifacts are clearly visible at the base and apex of the edge. Figure 10 shows the average of 100 axial sections of the reconstructed negative test object. The smoothed ESF from the same ROI as used for the positive test object is shown in figure 11. Any ripples from beam-hardening artifacts are not seen in this plot. The foil test objects were implemented in an earlier work on the same system with the same settings.¹¹ The results from that work are shown for the molybdenum foil test object (figure 13) and the resulting estimated LSF in figure 14, as well as for the aluminum foil test object (figure 15) and the resulting estimated LSF in figure 16.

For ease of visual comparison, the central 100 pixels of both ESFs are shown in figure 12. To facilitate comparison of the amount of spread, these ESFs have been rescaled so that the base is at 0 and the peak is at 1,

while the edges have been centered at 0 pixels on the x-axis. The normalization was accomplished by dividing the ESFs by their respective maximum grayscale value and then subtracting their minimum value, followed by recentering such that the crest of the edge is at pixel number 0.

Similarly, the central 20 pixels of the estimates of LSF are shown in figure 17, albeit with the pixel numbers converted to mm lengths using the pixel size conversion factor (.1 mm/pixel). As can be observed, the plots of each estimate of LSF present differences. The LSF curve from the foil is less noisy than that obtained from the other test objects, but exhibits a much wider spread in the molybdenum object. Because they track one another so closely, the LSFs from the aluminum foil and negative phantom were isolated and replotted in figure 18. The two LSFs follow one another in the central 1 mm, but the negative object's LSF appears to have much sharper shoulders, though this is uncertain due to noise.

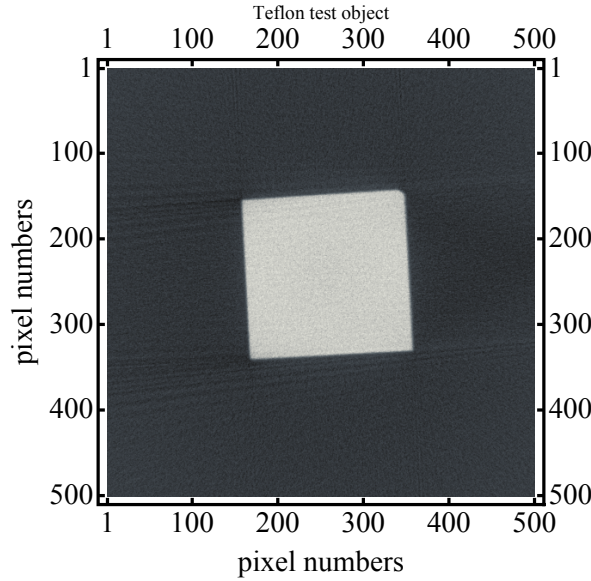


Figure 5: The average of 100 slices of the reconstructed positive test object.

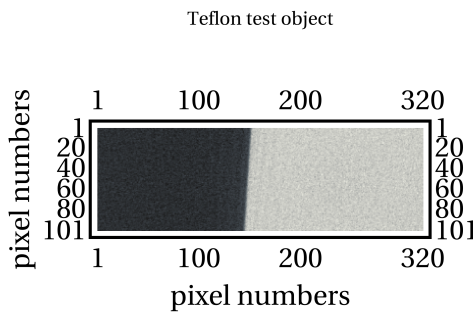


Figure 6: A region of interest from one edge of the positive cube test object. This is the reverse of the top edge.

4. DISCUSSION AND CONCLUSION

In this paper we present the LSF and ESF of four test objects that can be used for MTF estimation methods. Based on previous work,⁸ we expect that there will be frequency dependent differences in the results. Specifically, we expect that the edge methods will be superior for measuring low-frequency response, and that the slit method will be superior for measuring the high-frequency response. This will be explored further in future work.

When examining the ESF from each test object, the negative test object shows, as expected, fewer artifacts at the base and crest of the edge than the positive test object. However, the positive test object exhibits a sharper boundary between the two materials, as shown by a steeper slope to the edge, as seen in figure 12. To understand where this difference arises, it is important to first identify the sources that contribute to the spread of the edge. In this system, spread comes from the fact that the source has a finite size focal spot rather than a point source (generating focal spot unsharpness), the detector blur, potential geometric misalignments, and scatter generated within the phantom. The first three sources of spread are constant between the two test objects, and so we must conclude that the difference arises in how much generated scatter reaches the detector. Because the positive phantom is more attenuating than the negative phantom, it is reasonable to believe that some of the scattered photons generated in the surrounding water are absorbed in the higher-attenuating material. Effectively, fewer scattered photons in the edge regions reach the detector, and thus it appears that the image of the positive edge contains less spread. A similar effect can be seen in the asymmetry of the ESFs. With both the positive and negative test objects, tails at the base of the ESF (corresponding to the lower attenuation material) exhibit

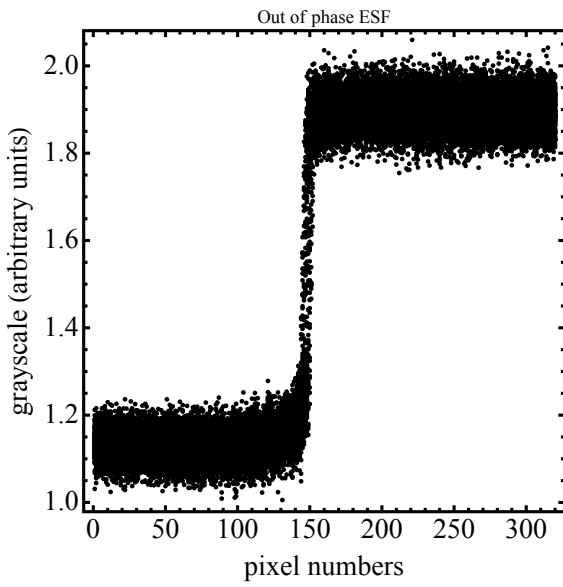


Figure 7: ESF estimates that are out of phase.

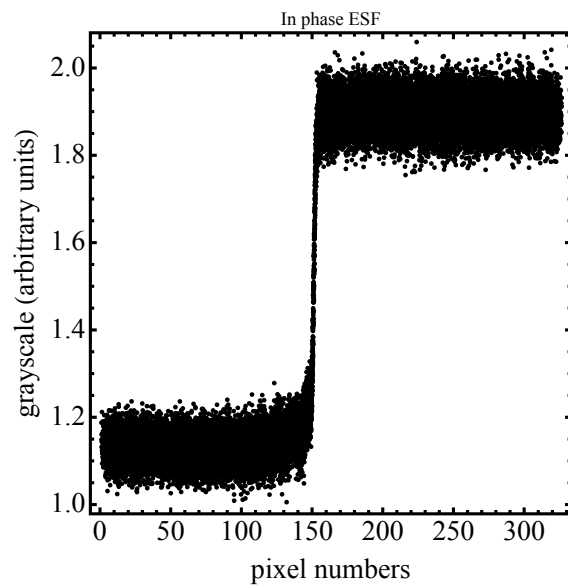


Figure 8: ESF estimates that have been shifted to be in phase.

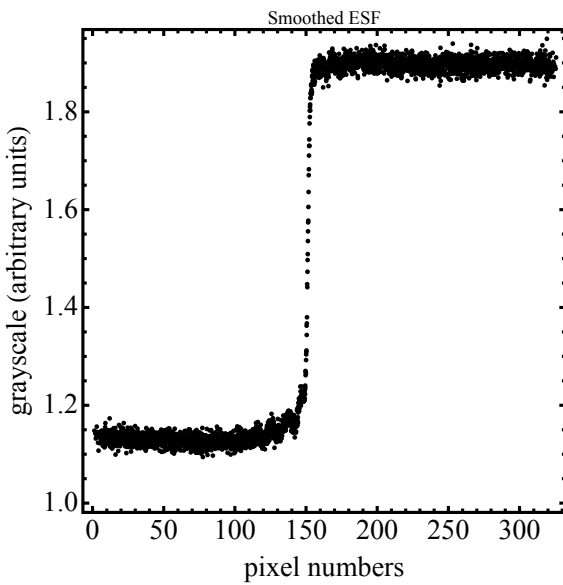


Figure 9: ESF estimates from the positive test object that have been smoothed by averaging every ten data points. Ripples from beam hardening artifacts are clearly visible at the base and apex of this edge.

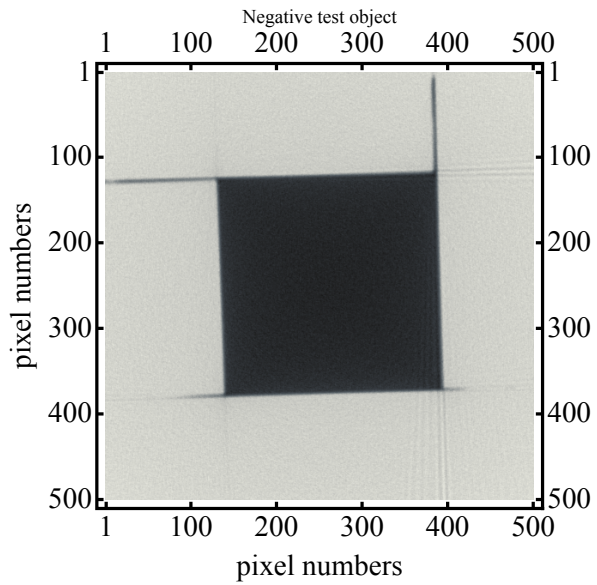


Figure 10: The average of 100 slices of the reconstructed negative test object.

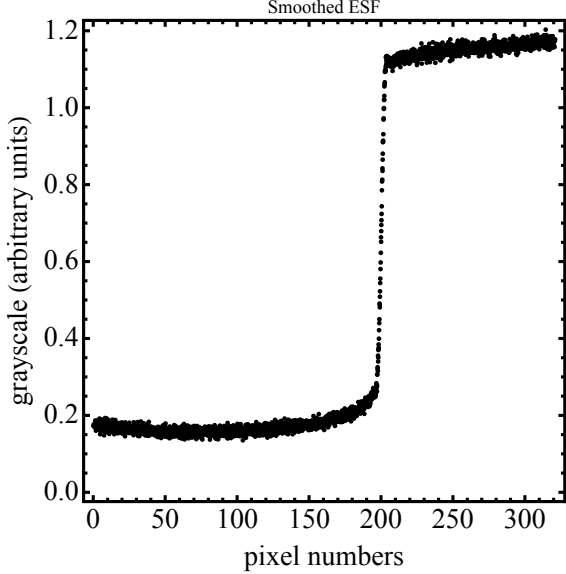


Figure 11: ESF estimates from the negative test object that have been smoothed by averaging every ten data points.

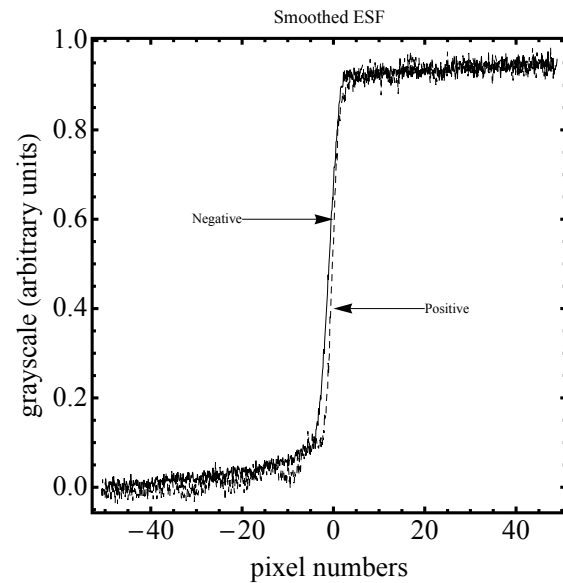


Figure 12: The central 100 pixels of both ESFs as obtained from the positive and negative test objects. The ESFs have been normalized and centered to allow for comparison of the relative amounts of spread.

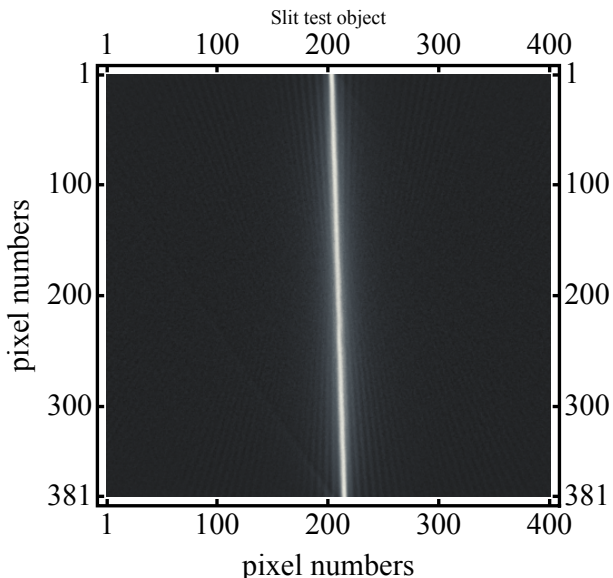


Figure 13: The average of 100 slices of the reconstructed molybdenum foil test object.

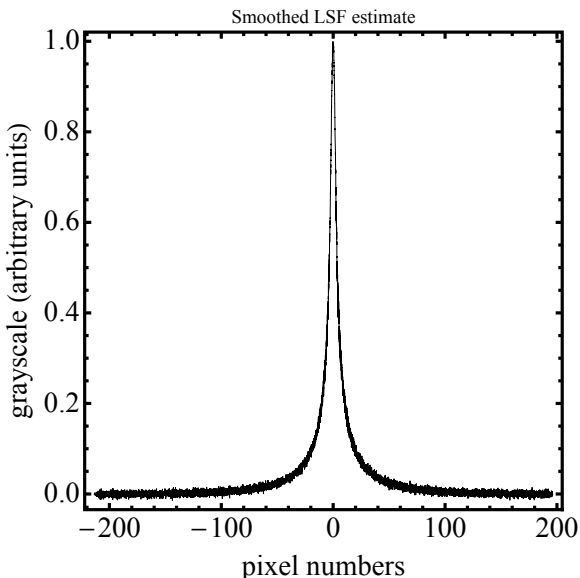
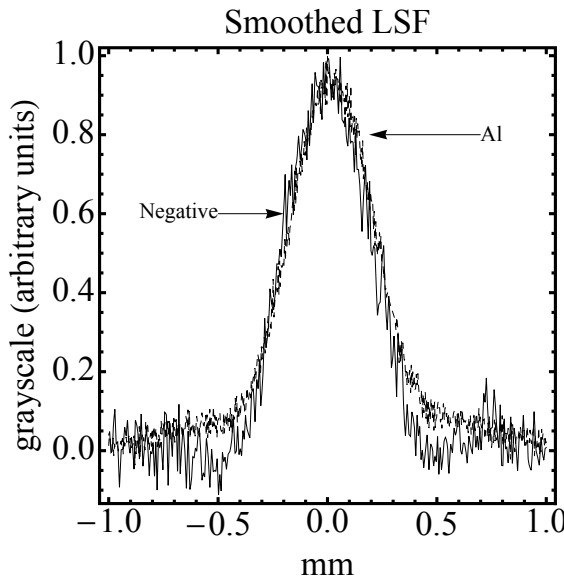
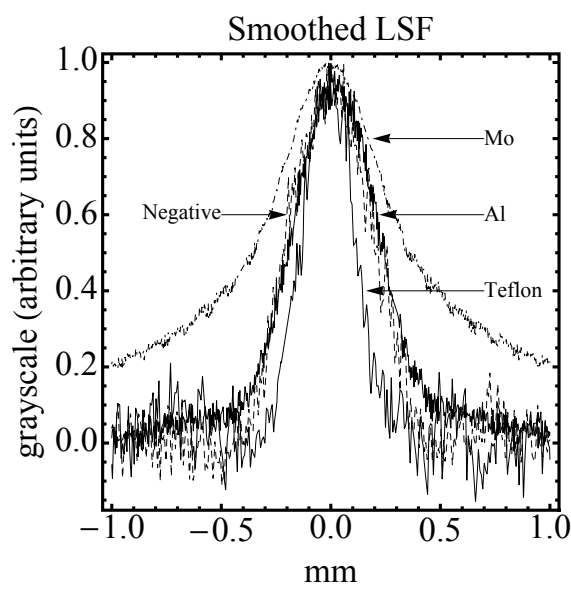
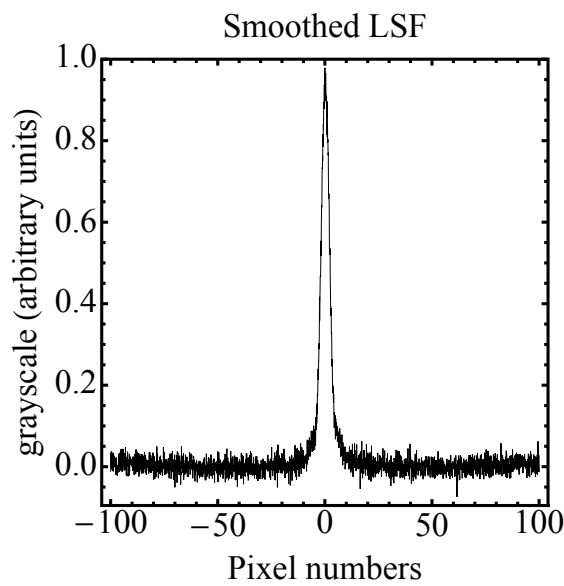
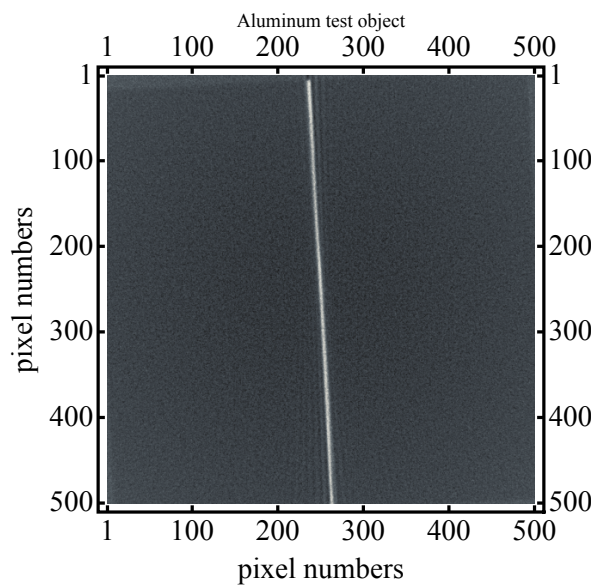


Figure 14: The average line profile of the reconstructed molybdenum foil test object.



longer, more slowly varying tails than the apex. It is our assumption therefore that these measured response functions are dependent on the material being imaged, with smaller spread if higher attenuation materials are used.

In figure 17, it appears that the slit method has less noise than the edge methods. This is explained by the method used to find the LSF from an ESF. To arrive at an LSF from an ESF, a derivative must be taken. The derivative operation multiplies the transfer function in the frequency domain by a factor of $i2\pi f$, amplifying high frequency noise. Additionally, we see in the plot that the molybdenum slit method results in a larger amount of spread in the LSF. This is due to two reasons. First, the line profile of the foil test object is not a true LSF, but rather the LSF convolved with a *rect* function of width equal to the width of the foil. However, the width of the molybdenum foil used was one fifth the size of a pixel, so the convolution of this *rect* function with the true LSF cannot account for the additional spread on its own. The second contributing factor is the radiodensity of the foil itself. At projection angles where the x-rays must travel through the length of the foil, significant beam hardening artifacts are introduced, greatly increasing the spread in the image. The last factor that contributes to the increased spread of the LSF (and indeed possibly affects all the test objects) is the fact that in order to reduce the noise multiple slices were averaged. The potential misalignment of the foil plane with the rotational axis can cause thickness of the the averaged foil reconstructed image to appear wider than it in fact is.

From these observations, we conclude that if one were to select a test object for estimating a spread function in tissues that are very similar to water, either the negative test cube object or the aluminum foil object is favored because one obtains an LSF that describes the scatter characteristics of the uniform water region. Because of its higher radiodensity (Teflon is approximately 990 HU), the positive cube might be a better approximation of the spread near more opaque structures, such as bone. The molybdenum foil method, because of the large number of metal artifacts and the difficulty in aligning with the rotational axis, results in a image with large spread of the LSF, and therefore we expect its applicability will be limited. Additionally, the edge method allows for the estimation of the spread function along the z-axis, which is difficult to achieve using the foil method. This is because, in order to avoid metal artifacts, foil slits used to measure the LSF along the z-axis must be exceedingly small in the x-y plane, making extraction of the presampling LSF a challenge. With careful alignment and use of the coronal or sagittal views in addition to axial views, the cube test object provides 6 tilted edges. Thus, one can extract four ESFs in the x-y plane, and two along the z-axis, and subsequently calculate the MTF in all three dimensions.

The results of this study are limited only to the center of the system we investigated. It is important to note that the LSF and ESF of a CT imaging system are not shift-invariant. This means that if off center measurements are taken, they are likely to differ from ESFs and LSFs measured here. However, the same methods can be used, and a profile of the imaging system's characteristics from center to periphery could be created.

Future work includes calculating the MTFs from these results and comparing the frequency dependent behaviors. Additionally, other phantoms for measuring a point spread function (PSF) are to be constructed and tested. These are to include bead-based and wire-based phantoms for acquiring the PSF in three dimensions and the PSF in the x-y plane, respectively.

REFERENCES

1. S. J. Shepard, P. Lin, J. M. Boone, D. D. Cody, J. R. Fisher, G. D. Frey, H. Glasser, J. E. Gray, A. G. Haus, L. V. Hefner, R. L. Holmes, R. J. Kobistek, F. N. Ranallo, P. L. Rauch, R. P. Rossi, J. A. Seibert, K. J. Strauss, O. H. Suleiman, J. R. Schenck, and S. K. Thompson, "Quality control in diagnostic radiology: Report of task group 12 diagnostic x-ray imaging committee," tech. rep., AAPM, 2002.
2. E. Samei, N. T. Ranger, J. T. Dobbins, and Y. Chen, "Intercomparison of methods for image quality characterization. I. Modulation transfer function," *Med. Phys.* **33**, pp. 1454–1465, 2006.
3. H. Fujita, D.-Y. Tsai, T. Itoh, K. Doi, J. Morishita, K. Ueda, and A. Ohtsuka, "A simple method for determining the modulation transfer function in digital radiography," *IEEE* **11**, pp. 34–38, 1992.
4. M. L. Giger and K. Doi, "Investigation of basic imaging properties in digital radiography. 1. modulation transfer function," *Med. Phys.* **11**, pp. 287–295, 1984.

5. E. L. Nickoloff, "Measurement of the PSF for a CT scanner: appropriate wire diameter and pixel size," *Phys. Med. Biol.* **33**, pp. 149–155, 1988.
6. J. M. Boone, "Determination of the presampled MTF in computed tomography," *Med. Phys.* **28**, pp. 356–360, 2001.
7. N. J. Schneiders and S. C. Bushong, "Single-step calculation of the MTF from the ERF," *Med. Phys.* **5**, pp. 31–33, 1978.
8. I. A. Cunningham and B. K. Reid, "Signal and noise in modulation transfer function determinations using the slit, wire, and edge techniques," *Med. Phys.* **19**, pp. 1037–1044, 1992.
9. I. S. Kyprianou, A. Badano, B. D. Gallas, and K. J. Myers, "Singular value description of a digital radiographic detector: Theory and measurements," *Medical Physics* **35**, pp. 4744–4756, 2008.
10. I. S. Kyprianou, A. Badano, B. D. Gallas, S. Park, and K. J. Myers., "A practical method for measuring the H matrix of digital x-ray and cone beam ct imaging systems," in *Society of Photo-Optical Instrumentation Engineers (SPIE) Conference Series*, **6142**, pp. 652–663, 2006.
11. C. C. Brunner, S. A. Hurowitz, S. F. Abboud, C. Hoeschen, and I. S. Kyprianou, "Noise characterization of computed tomography using the covariance matrix," in *SPIE Medical Imaging 2010: Physics of Medical Imaging*, E. Samei and N. J. Pelc, eds., **7622**(76224Z), 2010.
12. I. S. Kyprianou, S. Paquereault, B. D. Gallas, A. Badano, S. Park, and K. J. Myers, "Framework for determination of geometric parameters of a cone beam CT scanner for measuring the system response function and improved object reconstruction," in *Biomedical Imaging: Macro to Nano. 3rd IEEE International Symposium*, pp. 1248–1251, ISBI, IEEE, (Washinton DC), 2006.